Low-Speed LADRC for Permanent Magnet Synchronous Motor With High-Pass Speed Compensator

Qiangren Xu, Shuhua Fang, *Senior Member, IEEE*, Peng Wan, Yicheng Wang, and Demin Huang

***Abstract*— The operation of permanent magnet synchronous motors (PMSMs) is subject to many disturbances due to structural characteristics and operating situations. Particularly at low speeds, periodic disturbances, for instance, offset current error, cogging torque, etc., have a greater impact on the stable operation of the motor. For periodic disturbances, the conventional disturbance observer suffers from high delay and static error. Although the observer bandwidth can be increased to enhance the tracking ability to perturbations, this will introduce high-frequency noise at the same time. To solve these problems, an improved linear active disturbance rejection controller (LADRC) in this article is designed. By adding an error proportional feedback term to the extended state observer (ESO), the capability of the system to observe load perturbations is tremendously enhanced. A high-pass filter (HPF) is employed at the state error feedback (SEF) as a speed compensator. This method can reduce the speed of ripples feasibly without complex structures and tedious calculations. The stability of the proposed method is demonstrated by theoretical analysis, and both simulation and experimental results are given to verify the effectiveness of the proposed method.**

***Index Terms*— Extended state observer (ESO), linear active disturbance rejection control (LADRC), low-speed operation, periodic disturbance rejection.**

I. Introduction

PERMANENT magnet synchronous motor (PMSM) has been widely used in low-speed working conditions due to its simple structure, high efficiency, and high power density [1], [2]; however, when PMSM runs at low speed, there are periodic and aperiodic disturbances in the control system, such as flux harmonics, cogging torque, current measurement errors, dead time effect of inverter, load disturbances, and so on [3]. The low-frequency component, especially, results in speed fluctuation and poor control at low speeds [4].

Manuscript received 7 August 2023; revised 21 September 2023; accepted 18 October 2023. Date of publication 23 October 2023; date of current version 1 December 2023. This work was supported by the Joint Research Fund in Astronomy through Cooperative Agreement between the National Natural Science Foundation of China and Chinese Academy of Sciences under Grant U2031147. Recommended for publication by Associate Editor Sanjib (SSGE_M) K. Panda. *(Corresponding author: Shuhua Fang.)*

Qiangren Xu, Shuhua Fang, and Yicheng Wang are with the School of Electrical Engineering, Southeast University, Nanjing 210096, China (e-mail: xqr@seu.edu.cn; shfang@seu.edu.cn; 230218324@seu.edu.cn).

Peng Wan is with Jiangsu Electric Power Company Maintenance Branch, Nanjing 211100, China (e-mail: wan1997peng@163.com).

Demin Huang is with Inovance, Nanjing 211100, China (e-mail: 945013038@qq.com).

Color versions of one or more figures in this article are available at https://doi.org/10.1109/JESTPE.2023.3326858.

Digital Object Identifier 10.1109/JESTPE.2023.3326858

For low-speed PMSM drive systems, iterative learning control (ILC) is employed [5], which demonstrates that ILC achieves accurate reference tracking and total disturbance rejection. But this method will probably bring the risk of instability [6]. Proportional integral resonant (PIR) can reduce speed fluctuations, whereas it is only valid for the speed fluctuation caused by a specific perturbation [7]. Repetitive control (RC) in [8] and [9], are designed to minimize the periodic torque ripples to realize smooth speed; nevertheless, the control effect is affected by the frequency variation, and the robustness of the control system is poor [10]. Active disturbance rejection control (ADRC) does not distinguish modeling error (internal uncertainties) and external disturbance in the system and performs unified observation and compensation [11]. The adaption of ADRC in low-speed systems can better reflect its unique disturbance rejection advantages. Gao [12] simplifies ADRC to linear ADRC (LADRC) using linear extended state observer (LESO), which makes it extremely simple and practical, and the stability of the LADRC can be easily verified [13]. In [14], finite-time proportional (FTP) control combined with LESO is proposed with the comparison of PI and P+extended state observer (ESO). In order to increase the estimation accuracy of the fast-varying disturbance, a lot of research has been done. Godbole et al. [15] find that the higher order ESO offers improvement in the tracking of fast-varying sinusoidal disturbances. As the order and bandwidth of the observer increase, the ability of HESO to observe time-varying perturbations does increase, but it also makes the observations more sensitive to measurement noise [16]. To balance the accuracy of perturbation observations with the ability to suppress noise, a Kalman filter-type algorithm was employed to optimize the parameters of the gain [17]. Zhu et al. [18] proposed an adaptive switching high-order ESO with different error gains for transient state and steady state, which can weaken the effect of measurement noise on HESO at the cost of simplicity. A composite control law consisting of proportional feedback and disturbance feedforward compensation is proposed to pursue high multiple-disturbance rejection abilities [19]. To address the issues of limited degrees of freedom and insufficient antidisturbance capability in the LADRC, an enhanced approach called "Compensation Function Observer-based LADRC" (CFO-LADRC) is introduced in [20]. In [21], a composite control strategy is presented, which incorporates parameter-optimized ESOs in the speed

2168-6777 © 2023 IEEE. Personal use is permitted, but republication/redistribution requires IEEE permission.
See https://www.ieee.org/publications/rights/index.html for more information.

Authorized licensed use limited to: NANJING UNIVERSITY OF AERONAUTICS AND ASTRONAUTICS. Downloaded on May 30,2024 at 12:21:51 UTC from IEEE Xplore. Restrictions apply.

loop alongside sliding mode control and PI control with feed-forward compensation in the current loop.

The above studies have improved the operation of the motor to some extent but inevitably cause complications in the control system and algorithms. Based on previous studies and the above problems, this article proposes a novel speed-loop ADRC control method to ensure disturbances rejection and speed smoothness at low-speed operation of PMSM drives. A high-pass filter (HPF) is added to the state error feedback (SEF), and the error proportional feedback term is added to ESO. Compared with the traditional ADRC, this method expands the disturbance observation bandwidth and effectively enhances the ability to reject medium-frequency disturbances. The design of the proposed ADRC considers the local stability of the system, the disturbance rejection, and the robustness under the parametric variations.

This article is organized as follows. The analysis and effect of the low-frequency disturbance are presented in Section II. Section III introduces the design and problem of the speed-loop ADRC controller. Section IV presents the improvement of the speed-loop ADRC control method and the design of key parameters. In Section V, simulations and experiments verify the effectiveness of the proposed control method. Finally, the conclusion is drawn in Section VI.

II. Analysis and Effect of Periodic Disturbance

A. PMSM Model

The mathematical model of PMSM in the d-q reference frame can be written as

$$\begin{cases} u_d = R_s i_d + L_d \dfrac{di_d}{dt} - n_p \omega_m L_q i_q \\ u_q = R_s i_q + L_q \dfrac{di_q}{dt} + n_p \omega_m L_d i_d + n_p \omega_m \psi_f \end{cases} \tag{1}$$

where u_d and u_q are the stator voltages; i_d and i_q are the stator currents; R_s, L_d, L_q, and ψ_f are the stator resistance, d- and q-axes inductance, magnet flux linkage, respectively; n_p is the pole pairs of the rotor; ω_m is the mechanical angular speed.

The motion equation of PMSM can be expressed as

$$J\frac{d\omega_m}{dt} = T_e - T_L - B\omega_m \tag{2}$$

where J is the moment of inertia of the PMSM, T_e is the electromagnetic torque, T_L is the load torque, and B is the viscous coefficient.

With $i_d = 0$ control strategy, the equation of electromagnetic torque can be written as

$$T_e = \frac{3}{2} n_p \psi_f i_q. \tag{3}$$

B. Periodic Disturbance

The periodic disturbances of PMSM are mainly comprised of the torque resulting from offset current error, current scaling error, magnetic flux harmonics, cogging torque, and dead time effect.

1) Offset Current Error: Offset current error is the inherent dc-offset error between the true value of the current and the sensed value of the current sensor, which eventually results in a torque ripple. The measured currents of phases A–C, obtained through current sensors, can be represented according to [22]

$$\begin{cases} i_{as-\mathrm{AD}} = i_{as} + \Delta i_{as} \\ i_{bs-\mathrm{AD}} = i_{bs} + \Delta i_{bs} \\ i_{cs-\mathrm{AD}} = -(i_{as} + \Delta i_{as}) - (i_{bs} + \Delta i_{bs}) \end{cases} \tag{4}$$

where $i_{as-\mathrm{AD}}$, $i_{bs-\mathrm{AD}}$, and $i_{cs-\mathrm{AD}}$, are the measured currents of phases A–C, respectively. i_{as}, and i_{bs} are the actual currents of phases A and B. Δi_{as}, and Δi_{bs} are the offset current errors of phases A and B.

Following the *abc/dq* transformation, the measured q-axis current can be represented as:

$$\begin{cases} i_{qs-\mathrm{AD}} = i_{qs} + \Delta i_{qs_\mathrm{offset}} \\ \Delta i_{qs-\mathrm{offset}} = \dfrac{2}{\sqrt{3}}\sqrt{\Delta i_{as}^2 + \Delta i_{as}\Delta i_{bs} + \Delta i_{bs}^2}\cos(\theta_e + \alpha) \end{cases} \tag{5}$$

where $i_{qs-\mathrm{AD}}$ is the measured q-axis current, i_{qs} is the actual q-axis current, $\Delta i_{qs-\mathrm{offset}}$ is the q-axis offset current, θ_e is the electrical angle, and $\theta_e = 2\pi f_e t$; α is the angle related to Δi_{as} and Δi_{bs}; f_e is the stator electrical frequency.

Combining (5) with (3), the torque caused by offset current error $\Delta T_{\mathrm{offset}}$ can be expressed as

$$\Delta T_{\mathrm{offset}} = \frac{2}{\sqrt{3}} n_p \psi_f \sqrt{\Delta i_{as}^2 + \Delta i_{as}\Delta i_{bs} + \Delta i_{bs}^2}\cos(\theta_e + \alpha). \tag{6}$$

2) Current Scaling Error: The gain mismatch of the current sensor results in a deviation between the current detection value and the real value, which further forms current disturbance. The measured currents of phases A and B, obtained through current sensors according to [23] and [24], can be rewritten as

$$\begin{cases} i_{as-\mathrm{AD}} = I\cos\theta_e \\ i_{bs-\mathrm{AD}} = I\cos\left(\theta_e - \dfrac{2\pi}{3}\right) \end{cases} \tag{7}$$

where I is the amplitude of phase current. Considering the gain mismatch of the current sensor, the actual currents of phases A and B can be rewritten as

$$\begin{cases} i_{as} = I\cos\theta_e / k_a \\ i_{bs} = I\cos\left(\theta_e - \dfrac{2\pi}{3}\right)/k_b \end{cases} \tag{8}$$

where k_a and k_b are the current calibration coefficients. Following the *abc/dq* transformation, the q-axis current error $\Delta i_{qs-\mathrm{scale}}$ can be represented as

$$\Delta i_{qs-\mathrm{scale}} = \left(\frac{k_a - k_b}{k_a k_b}\right)\frac{I}{\sqrt{3}}\left[\cos\left(2\omega_e t + \frac{\pi}{3}\right) + \frac{1}{2}\right]. \tag{9}$$

By combining (9) with (3), the torque caused by the current scaling error $\Delta T_{\mathrm{scale}}$ can be expressed as

$$\Delta T_{\mathrm{scale}} = n_p \psi_f \left(\frac{k_a - k_b}{k_a k_b}\right)\frac{I}{\sqrt{3}}\left[\cos\left(2\omega_e t + \frac{\pi}{3}\right) + \frac{1}{2}\right]. \tag{10}$$

Authorized licensed use limited to: NANJING UNIVERSITY OF AERONAUTICS AND ASTRONAUTICS. Downloaded on May 30,2024 at 12:21:51 UTC from IEEE Xplore. Restrictions apply.

3) Cogging Torque: The cogging torque generated by uneven permeability in the air gap due to the nonuniform rotation of the motor after stator slotting can be expressed as (11) according to [7] and [25]

$$T_c = K_c \sin(N_c\theta + \pi) \tag{11}$$

where T_c is the cogging torque; K_c is the amplitude of cogging torque; θ is the rotor position; N_c is the minimum common multiple of rotor pole pairs and stator slots.

4) Flux Harmonic: Problems such as iron core saturation, stator slotting, and asymmetry of actual processing and installation make the magnetic flux density of the air gap unable to fully realize a sinusoidal distribution in space, so there are various harmonic components in the flux linkage. In the *d-q* frame, the corresponding harmonics appear as the sixth, 12th, and other multiples of the sixth harmonics, which can be expressed as

$$\psi_{dm} = \psi_{d0} + \psi_{d6}\cos 6\theta_e + \psi_{d12}\cos 12\theta_e + \cdots \tag{12}$$

where ψ_{dm} is the total flux linkage, ψ_{d0} is the fundamental component of the flux linkage, and ψ_{d6} and ψ_{d12} are the sixth and 12th harmonics components, respectively.

The torque considering flux harmonic, according to [26] and [27], can be expressed as

$$T_m = T_0 + T_6\cos 6\theta_e + T_{12}\cos 12\theta_e + \cdots \tag{13}$$

where T_m is the total torque, T_0 is the fundamental component, and T_6 and T_{12} are the sixth and 12th harmonics components.

5) Dead Time Effect: Because of the presence of dead time, a reduction in the output voltage of the inverter occurs, and harmonic distortion is generated, leading to voltage distortion at the output. The voltage error in *dq*-axes, according to [28] and [29], can be expressed as

$$\begin{cases} \Delta u_{d,\text{dead}} = \dfrac{4U_{\text{dead}}}{\pi}\left[\displaystyle\sum_{n=1}^{\infty}\dfrac{2}{36n^2-1}\sin(6n\omega_e t)\right] \\ \Delta u_{q,\text{dead}} = \dfrac{4U_{\text{dead}}}{\pi}\left[-1+\displaystyle\sum_{n=1}^{\infty}\dfrac{2}{36n^2-1}\cos(6n\omega_e t)\right] \\ U_{\text{dead}} = U_{\text{dc}}\dfrac{T_d + T_{\text{on}} - T_{\text{off}}}{2T_s} \end{cases} \tag{14}$$

where $\Delta u_{d,\text{dead}}$ and $\Delta u_{q,\text{dead}}$ are the stator voltage component caused by dead time. U_{dead} and U_{dc} are the average voltage due to dead time effect and bus voltage. T_{on}, T_{off}, T_d, and T_s denote the turn-on time, turn-off time, dead time, and switching period, respectively.

III. Conventional Speed-Loop LADRC

The conventional ADRC consists of tracking differentiator (TD), ESO, SEF, and compensation of disturbance estimation. Reasonable TD can track the input signal as quickly as possible and give the approximate differential signal. ESO is the core of the ADRC, expanding the disturbance into a new state variable and constructing the state observer according to the mathematical model and the observation error. SEF performs linear or nonlinear feedback on the state variable error and outputs the control quantity. SEF closely affects the dynamic response performance and steady-state control accuracy. The compensation of disturbance estimation is to use the disturbance observation value of ESO to perform feedforward compensation to realize disturbance decoupling. The design of each part is analyzed as follows.

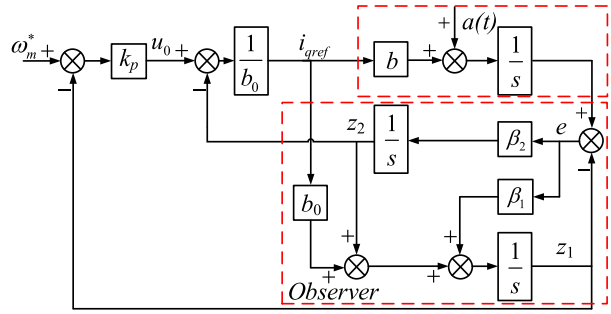

Fig. 1. Structure of the conventional LADRC.

A. Design of Speed-Loop LADRC

The design procedure of the speed LADRC controller is addressed as follows. In order to simplify the structure of ADRC and reduce the difficulty of parameter design, TD can be eliminated [12] directly using ω_m^* as the reference mechanical angular speed input. Fig. 1 shows the structure of the conventional LADRC.

From (2), the state equation can be established as

$$\dot{\omega}_m = bi_q + a \tag{15}$$

where b is the nominal value of torque coefficient and $b = 1.5n_p\psi_f/J$; a is the total disturbance in the built model, $a = -(T_L + B\omega_m)/J$.

Expanding a in (15) into a new state variable x_2, the state space equation of the system can be written as

$$\begin{cases} \dot{x}_1 = x_2 + bu \\ \dot{x}_2 = \dot{a} \\ y = x_1 \end{cases} \tag{16}$$

where x_1, x_2 are the state variables of the system, x_1 is the motor speed, y is the system output, u is the control variable of the system, $u = i_{q\text{ref}}$.

LESO is designed as

$$\begin{cases} e = y - z_1 \\ \dot{z}_1 = z_2 + \beta_1 e + b_0 u \\ \dot{z}_2 = \beta_2 e \end{cases} \tag{17}$$

where e is the observation error of mechanical angular speed, $b_0 = b = 1.5n_p\psi_f/J$; z_1, z_2 are the estimates of the motor speed x_1 and the total system disturbance x_2, respectively; and β_1 and β_2 are the state observer gains to be designed.

The characteristic equation of the observer coefficient matrix is

$$s^2 + \beta_1 s + \beta_2 = 0. \tag{18}$$

In order to ensure the stable performance of the observer, the eigenvalues of the observer coefficient matrix must all be distributed in the left half-plane of the s-domain coordinate plane,

Authorized licensed use limited to: NANJING UNIVERSITY OF AERONAUTICS AND ASTRONAUTICS. Downloaded on May 30,2024 at 12:21:51 UTC from IEEE Xplore. Restrictions apply.

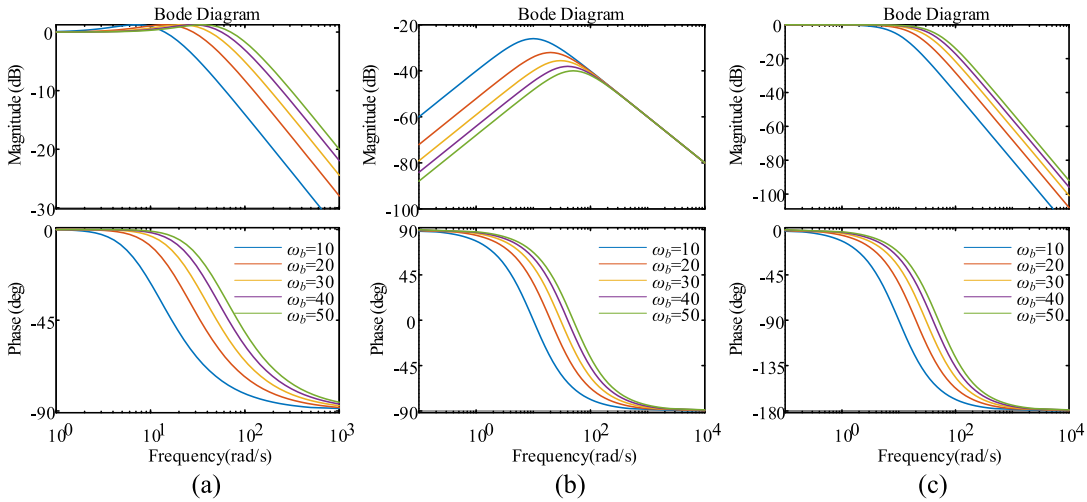

Fig. 2. Bode diagram of the transfer function of the traditional LESO. (a) Speed observation z_1 to ω_m, (b) speed observation z_1 to $b_0 i_q$, and (c) disturbance observation z_2 to a.

so β_1 and β_2 must be real numbers, not less than zero. To simplify the parameter design, the bandwidth method in [12] is used to determine the gain of the ESO, β_1 and β_2 can be chosen as

$$\beta_1 = 2\omega_b, \quad \beta_2 = \omega_b^2 \tag{19}$$

where ω_b is the bandwidth of the ESO. ω_b can be determined according to the dynamic performance and steady-state performance requirements of the system. An appropriate ω_b is beneficial to improve the system observation performance and further improve the disturbance suppression capability.

B. Problems of LADRC

The disturbance observation value can be obtained after an integral operation of e, which reduces the speed and effectiveness of perturbation observation.

The closed-loop transfer function of the observed values z_1 and z_2 in the observer can be written as

$$\begin{cases} z_1(s) = \dfrac{\beta_1 s + \beta_2}{s^2 + \beta_1 s + \beta_2}\omega_m(s) + \dfrac{s}{s^2 + \beta_1 s + \beta_2} b_0 i_q(s) \\ z_2(s) = \dfrac{\beta_2}{s^2 + \beta_1 s + \beta_2} a(s). \end{cases} \tag{20}$$

According to (20), z_1 tracks rotor speed, but the disturbance in the q-axis current will also be introduced to z_1, which will result in bias to the estimated value.

C. Parametric Analysis

Based on (20), the Bode diagrams of ω_m and $b_0 i_q$ against z_1 are, respectively, shown in Fig. 2(a) and (b). The Bode diagram of disturbance observation is shown in Fig. 2(c). As shown in Fig. 2(c), the ESO has a high phase delay for the observation of disturbances; although increasing ω_b can mitigate the phase delay, it yields a high noise to the speed observation.

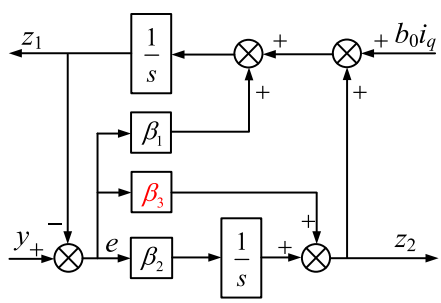

Fig. 3. Structural diagram of improved ESO.

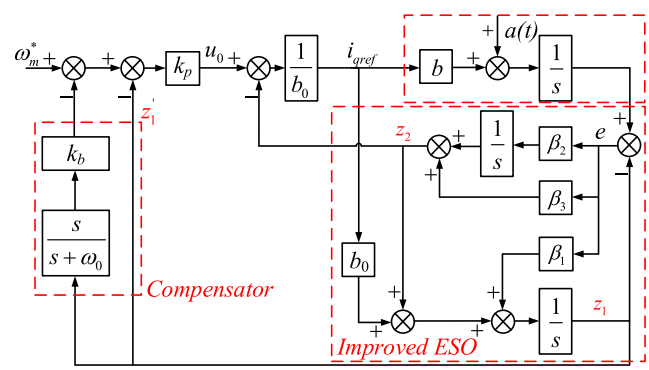

Fig. 4. Diagram of the proposed control system.

IV. Improved Speed-Loop LADRC

The speed-loop LADRC is improved with the improved LESO- and HPF-based speed compensator, which will enhance the observation ability and periodic disturbance rejection performance.

A. Design of Improved LADRC

Since the traditional LESO is built on the base of β_1 and β_2, as shown in (17), β_3 can be added in the disturbance observation, as shown in Fig. 3, which is the gain coefficient of the state observation error. Fig. 4 shows the simplified control system in which PI control is adopted to the current loop.

Authorized licensed use limited to: NANJING UNIVERSITY OF AERONAUTICS AND ASTRONAUTICS. Downloaded on May 30,2024 at 12:21:51 UTC from IEEE Xplore. Restrictions apply.

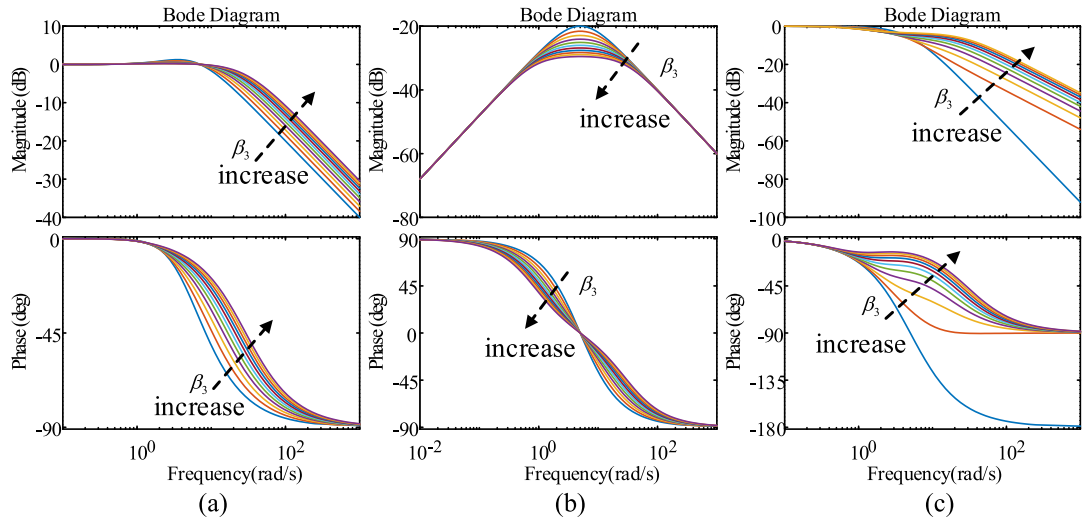

Fig. 5. Bode diagram of the transfer function of the proposed LESO. (a) Speed observation z_1 to ω_m, (b) speed observation z_1 to b_{0iq}, and (c) disturbance observation z_2 to a.

The state space function of improved LESO is designed as

$$\begin{cases} e = y - z_1 \\ \dot{z}_1 = z_2 + \beta_1 e + b_0 u \\ \dot{z}_2 = \beta_2 e + \beta_3 \dot{e} \end{cases} \tag{21}$$

The transfer function of improved LESO can be expressed as

$$\begin{cases} z_1(s) = \dfrac{[(\beta_1+\beta_3)s+\beta_2]\omega_m(s) + s b_0 i_q(s)}{s^2+(\beta_1+\beta_3)s+\beta_2} \\ z_2(s) = \dfrac{\beta_3 s + \beta_2}{s^2+(\beta_1+\beta_3)s+\beta_2} a(s) \end{cases} \tag{22}$$

where $\beta_1 + \beta_3 = 2\omega_b$, $\beta_2 = \omega_b^2$, ω_b is the bandwidth of the improved ESO.

According to (22), in the speed observation, the introduction of β_3 not only improves rotor speed tracking performance but also reduces the influence of q-axis current. In disturbance observation, β_3 increases the numerator order so as to improve the observation performance for high-frequency disturbances.

Fig. 5 shows the Bode diagram of the transfer function of the proposed LESO with β_3 changing from 0 to 200. From Fig. 5(a) and (b), as β_3 increases, the ability of the observer to observe the speed increases and the suppression in q-axis current fluctuations by the observer increases, whereas high-frequency noise is introduced into the observed speed, which, in turn, affects the control performance.

Fig. 5(c) shows that the ability of disturbance observation is improved with the introduction of β_3. More importantly, the phase delay of the observer for disturbance observation is significantly reduced.

As analyzed above, with the increase of β_3, high-frequency fluctuations will, however, occur and the system will overshoot, so β_3 should not be set too large.

B. Design of Speed Compensator

The tracking performance of the observer can be enhanced by increasing the bandwidth of LESO; however, it is important to note that the bandwidth cannot be increased indefinitely. One of the main factors limiting the increase in LESO bandwidth is the introduction of high-frequency noise. As the bandwidth increases, the amplification effect of high-frequency noise becomes stronger, thereby subjecting the system to greater disturbances at high frequencies. By incorporating HPF in the velocity compensator, the high-frequency disturbance component caused by the increased bandwidth can be attenuated. Consequently, this improves the dynamic response and steady-state control precision of the system.

Based on the linear feedback, HPF can be used to extract the intermediate frequency and high-frequency signals from the observed rotor speed. So, HPF can be employed to eliminate harmonic disturbances in the speed loop. The error feedback control law can be expressed as

$$\begin{cases} z_1' = k_b \dfrac{s}{s+\omega_0} z_1 + z_1 \\ u_0 = k_p\left(v - k_b \dfrac{s}{s+\omega_0} z_1 - z_1\right) \\ u = \dfrac{u_0 - z_2}{b_0} \end{cases} \tag{23}$$

where z_1' is the composite compensator with a HPF, k_p is the gain coefficient of the error feedback, and k_b and ω_0 are the gain and cut-off frequency of HPF. For convenience, v is used instead of the reference speed ω_m^* in the following derivation.

The improved LESO transfer function (22) can be substituted into the feedback control law (16) as

$$\begin{aligned} b_0 u = {} & k_p v - k_p \frac{(k_b+1)s+\omega_0}{s+\omega_0} \frac{(\beta_1+\beta_3)s+\beta_2}{s^2+(\beta_1+\beta_3)s+\beta_2}\omega_m \\ & + k_p \frac{(k_b+1)s+\omega_0}{s+\omega_0} \frac{s}{s^2+(\beta_1+\beta_3)s+\beta_2} b_0 u \\ & - \frac{\beta_3 s+\beta_2}{s^2+(\beta_1+\beta_3)s+\beta_2} a. \end{aligned} \tag{24}$$

Authorized licensed use limited to: NANJING UNIVERSITY OF AERONAUTICS AND ASTRONAUTICS. Downloaded on May 30,2024 at 12:21:51 UTC from IEEE Xplore. Restrictions apply.

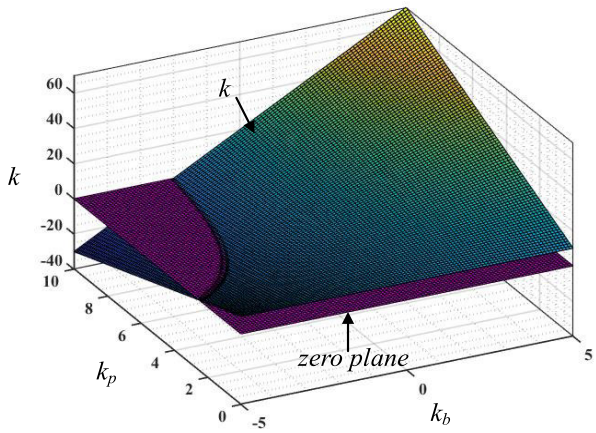

Fig. 6. Value of k varying with k_p and k_b.

The b_0u items can be sorted out as

$$b_0u = \frac{k_p v - k_p \frac{(k_b+1)s+\omega_0}{s+\omega_0} \frac{(\beta_1+\beta_3)s+\beta_2}{s^2+(\beta_1+\beta_3)s+\beta_2}\omega_m}{1 + k_p \frac{(k_b+1)s+\omega_0}{s+\omega_0} \frac{s}{s^2+(\beta_1+\beta_3)s+\beta_2}} - \frac{\frac{\beta_3 s+\beta_2}{s^2+(\beta_1+\beta_3)s+\beta_2} a}{1 + k_p \frac{(k_b+1)s+\omega_0}{s+\omega_0} \frac{s}{s^2+(\beta_1+\beta_3)s+\beta_2}}. \tag{25}$$

It is assumed that $b = b_0$, and (25) is substituted into (15) to eliminate the bu term, and therefore, the transfer function of the simplified control system can be written as

$$\omega_m = \frac{k_p(s+\omega_0)}{s^2 + \big((k_b+1)k_p + \omega_0\big)s + k_p\omega_0}\omega_m^* + \frac{s^3+(\omega_0+\beta_1)s^2+(k_pk_b+k_p+\omega_0)s+k_p\omega_0}{\big(s^2+(\beta_1+\beta_3)s+\beta_2\big)\big[s^2+\big((k_b+1)k_p+\omega_0\big)s+k_p\omega_0\big]}a. \tag{26}$$

C. Stability Analysis and Parameter Design

According to (26), the characteristic equation of the simplified control system can be written as

$$\big(s^2+(\beta_1+\beta_3)s+\beta_2\big)\big[s^2+\big((k_b+1)k_p+\omega_0\big)s+k_p\omega_0\big] = 0. \tag{27}$$

According to (19), when LESO is stable, it only needs to ensure that the roots of (27) are all in the left half-plane of the s-domain, then one can have

$$\begin{cases} s^2 + \big((k_b+1)k_p+\omega_0\big)s + k_p\omega_0 = 0 \\ k = (k_b+1)k_p + \omega_0. \end{cases} \tag{28}$$

Fig. 6 shows the value of k varying with k_p and k_b. According to the Rouse–Hurwitz theorem, it can be obtained that when $k_p > 0$, $\omega_0 > 0$, $k > 0$, the roots of (27) are always located in the left half-plane of the s domain, the system is stable.

Considering β_3, the ratio of the observed value $z_2(s)$ to the disturbance $a(s)$ and the ratio of the output speed $\omega_m(s)$ to the disturbance $a(s)$ can be expressed as

$$\begin{cases} \dfrac{z_2(s)}{a(s)} = \dfrac{\beta_3 s+\beta_2}{s^2+(\beta_1+\beta_3)s+\beta_2} \\ \dfrac{\omega_m(s)}{a(s)} = \dfrac{s^3+(\omega_0+\beta_1)s^2+(k_pk_b+k_p+\omega_0)s+k_p\omega_0}{\big(s^2+(\beta_1+\beta_3)s+\beta_2\big)\big[s^2+\big((k_b+1)k_p+\omega_0\big)s+k_p\omega_0\big]} \end{cases} \tag{29}$$

where $\beta_1 + \beta_3 = 2\omega_b$, $\omega_b = 200$, $k_b = 10$, $k_p = 2$, $\omega_0 = 10$.

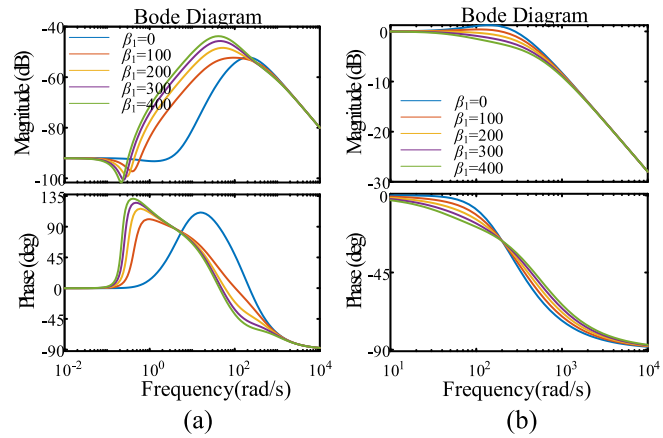

Fig. 7. Bode diagram of the transfer function varying with β_1. (a) z_2 and (b) ω_m.

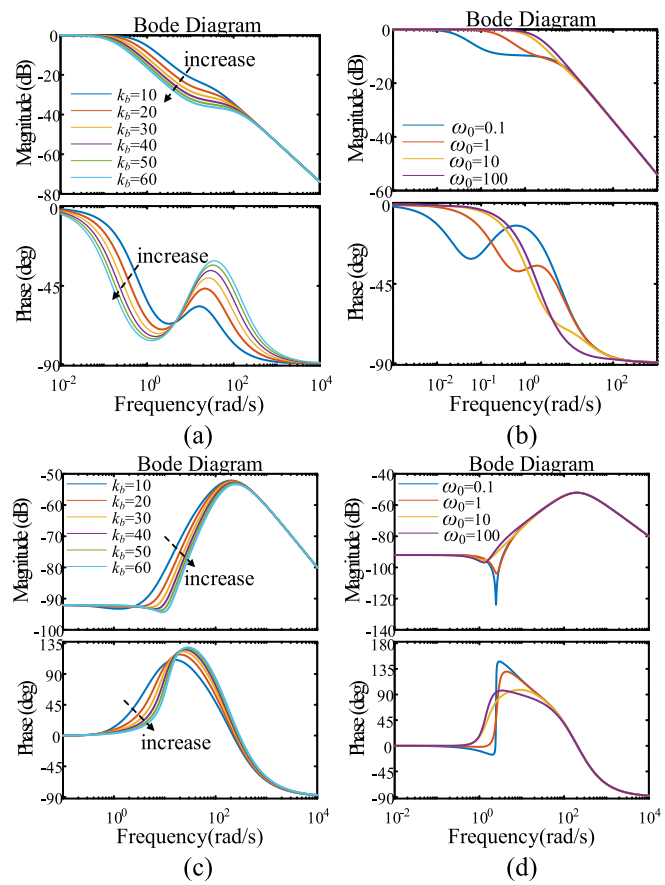

Fig. 8. Bode diagram of the speed observation and disturbance rejection transfer function with one variable parameter. (a) Speed observation with k_b, (b) speed observation with ω_0, (c) disturbance rejection with k_b, and (d) disturbance rejection with ω_0.

Authorized licensed use limited to: NANJING UNIVERSITY OF AERONAUTICS AND ASTRONAUTICS. Downloaded on May 30,2024 at 12:21:51 UTC from IEEE Xplore. Restrictions apply.

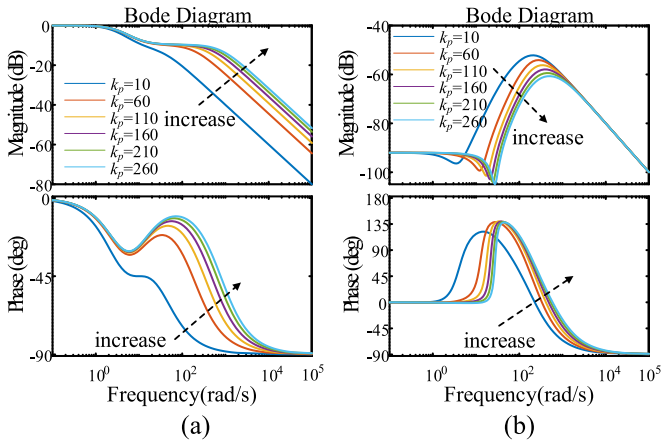

Fig. 9. Bode diagram of the speed observation and disturbance rejection transfer function with k_p. (a) Speed observation and (b) disturbance rejection.

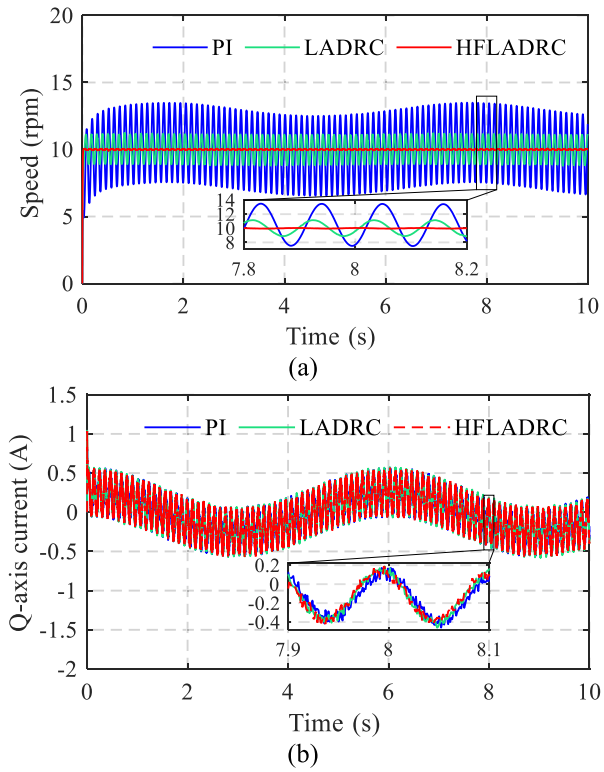

Fig. 10. Performance of PI, LADRC, and HFLADRC at 10 r/min. (a) Speed and (b) q-axis current.

The Bode diagram of (29) is shown in Fig. 7. When $\beta_1 = 0$, the observer has the largest bandwidth for perturbation observations and the lowest phase delay; at the same time, the speed has the lowest bandwidth and gain for the perturbation transfer function, thus $\beta_1 = 0$ and $\beta_3 = 2\omega_b$.

Fig. 8(b) and (d) are the Bode diagrams when k_b is 2, and ω_0 is variable. ω_0 has a great influence on the tracking performance and disturbance rejection capability. When ω_0 increases, the speed tracking range of the system increases; however, an increase in ω_0 leads to a reduction in the ability to suppress disturbances. After ω_0 reaches 10, further increases in ω_0 have little effect on the observed speed.

Fig. 9 shows the Bode diagram of the speed observation and disturbance rejection transfer function change with k_p.

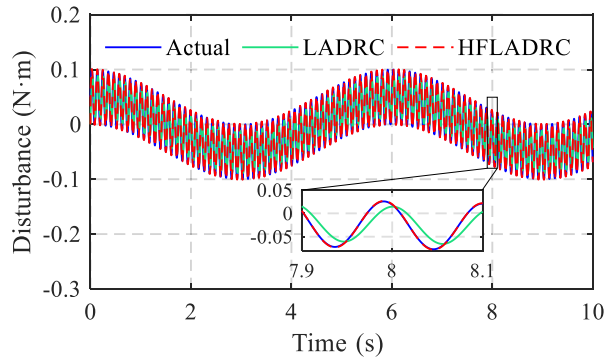

Fig. 11. Disturbance observation performance of LADRC and HFLADRC at 10 r/min.

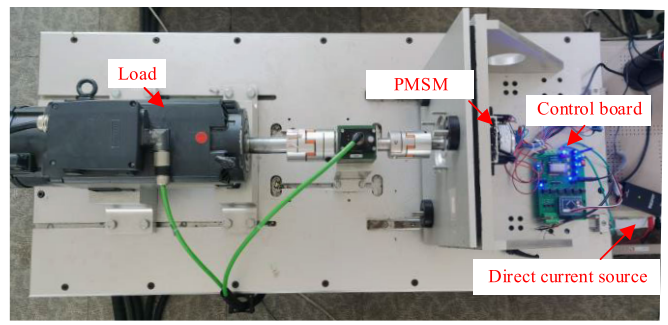

Fig. 12. Experimental platform.

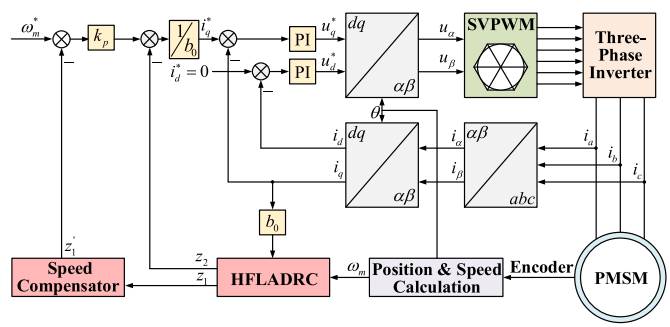

Fig. 13. Block diagram of the control system.

As k_p increases, the control system's ability to observe speed and suppress disturbances is enhanced, whereas such a change in these two abilities gradually slows down after the value of k_p reaches 200.

V. Simulation and Experimental Results

A. Simulation Results

The effectiveness of the proposed method will be evaluated by comparing the performance of the system using traditional PI, conventional LADRC, and HPF-based LADRC (HFLADRC). The simulation models are built in MATLAB/Simulink.

The parameters of the speed PI controller are $k_{ps} = 1$ and $k_{is} = 50$. The parameters of the current PI controller are $k_{pc} = 3.48$ and $k_{ic} = 12$. The parameter design of the traditional LADRC is the same as that of HFLADRC. The parameters of HFLADRC are $k_b = 1$, $k_p = 100$, $\omega_0 = 1$, $\omega_b = 200$. The parameters above are selected at a resolution

Authorized licensed use limited to: NANJING UNIVERSITY OF AERONAUTICS AND ASTRONAUTICS. Downloaded on May 30,2024 at 12:21:51 UTC from IEEE Xplore. Restrictions apply.

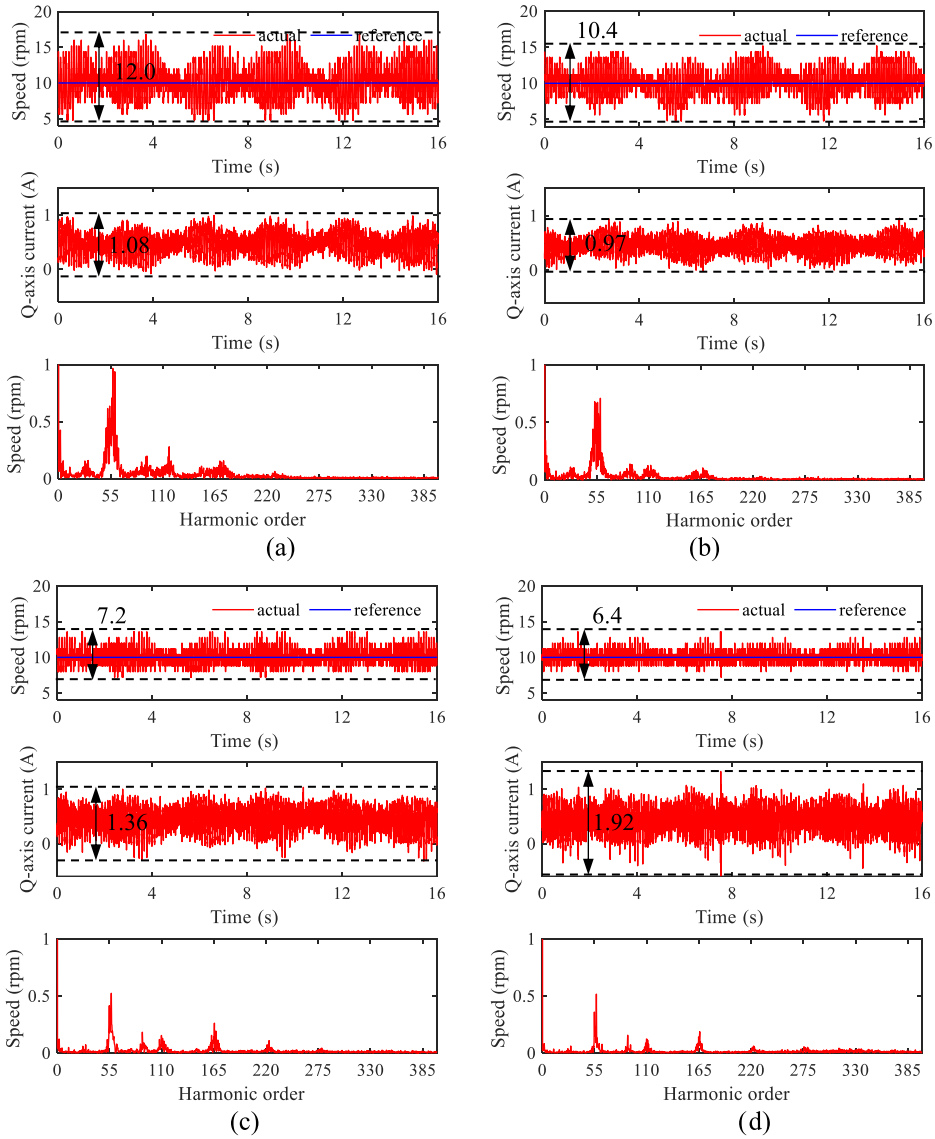

Fig. 14. Experimental results of four control methods at 10 r/min. (a) PI, (b) robust ILC, (c) LADRC, and (d) HFLADRC.

of 10/min. Table I lists the parameters of the motor in the simulation.

Two periodic disturbances, one at the mechanical angular frequency and the other at 55 times that frequency, are added to the simulation to evaluate the ability of the control scheme to suppress the disturbance. Both disturbances had an amplitude of 0.05 Nm. Fig. 10(a) and (b) present the speed and q-axis current performance of PI, LADRC, and HFLADRC at 10 r/min. It can be seen that the speed waveform of the PI controller exhibits two types of fluctuations corresponding to mechanical and electrical angular frequencies simultaneously. The fluctuation of speed under LADRC is approximately 3 r/min, and there is no obvious low-frequency fluctuation related to mechanical frequency. HFLADRC has the best speed performance, with almost no low-frequency fluctuation and minimal high-frequency fluctuation amplitude, proving the effectiveness of the proposed method under complex disturbances. The q-axis currents of the three control schemes have almost the same performance.

TABLE I
PARAMETERS OF PMSM

Symbol	Characteristics	Values
R_s	Stator resistance	3.5Ω
L	dq-axis inductance	7mH
P_n	Rated power	100W
I_n	Rated current	10A
n_p	Pole Pairs	55
J	Moment of inertia	8×10^{-4}kg·m^2
B	Friction coefficient	3.3×10^{-3}N·m·s
ψ_f	PM flux linkage	0.0024Wb

Fig. 11 illustrates the disturbance observation performance of LADRC and HFLADRC at 10 r/min. It can be seen that HFADRC exhibits excellent observation performance for

Authorized licensed use limited to: NANJING UNIVERSITY OF AERONAUTICS AND ASTRONAUTICS. Downloaded on May 30,2024 at 12:21:51 UTC from IEEE Xplore. Restrictions apply.

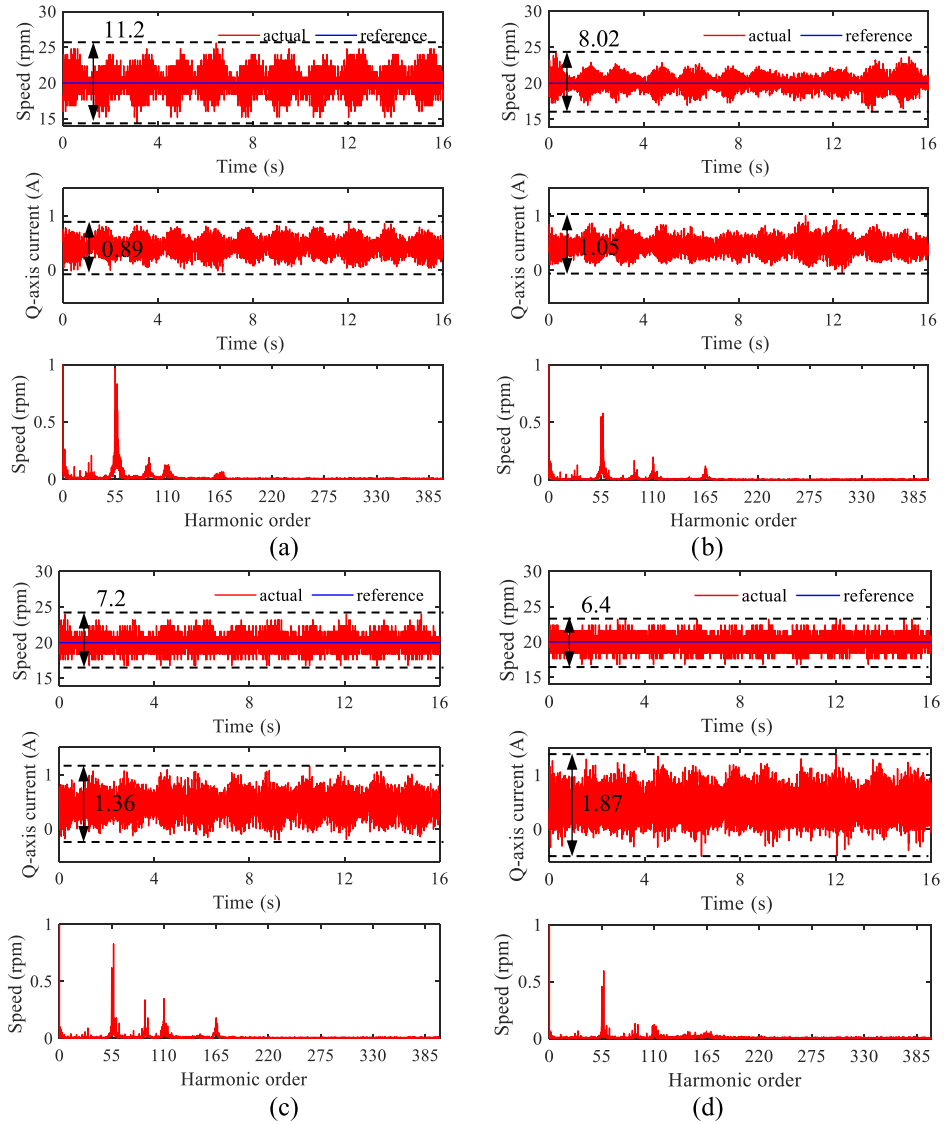

Fig. 15. Experimental results of four control methods at 20 r/min. (a) PI, (b) robust ILC, (c) LADRC, and (d) HFLADRC.

disturbances, accurately tracking both amplitude and phase; LADRC, on the other hand, has a 0.01 Nm amplitude error and a certain phase delay, resulting in inferior speed performance compared to HFLADRC.

B. Experiment Results

The proposed HFLADRC control strategy discussed in Section III is tested on an experimental drive system. As shown in Fig. 12, the experimental platform includes a PMSM, a load motor, and a control board, which includes a sampling circuit, power circuit, and control circuit. The current sensor CC6904SO is used to convert the current value into a voltage value and is read by A/D conversion in the control circuit. In the power circuit, the bus voltage of the three-phase inverter is set to 50 V by the direct current source supply. The control circuit includes the control chip STM32F407 and a 10 000 pulse per resolution encoder for speed measurement. The sampling frequency of the speed loop and current loop is 2 and 10 kHz. The parameters of the controlled motor are listed in Table I. Fig. 13 shows the whole control block diagram.

The performance criterion to evaluate the effectiveness of the proposed scheme for speed ripple reduction is the speed ripple factor (SRF), which is assessed as a percentage of deviation from the reference value

$$\mathrm{SRF} = \frac{\omega_{m_pk-pk}}{\omega_m^{\mathrm{ref}}} 100(\%) \tag{30}$$

where ω_{m_pk-pk} is the peak-to-peak speed ripples and ω_m^{ref} is the reference speed.

Fig. 14 shows the experimental results of the speed performance, q-axis currents, and speed spectrum of different control strategies (PI, robust ILC in [6], LADRC, and HFLADRC) with no load at 10 r/min. It can be seen that the PI controller cannot suppress the speed fluctuation, and the maximum speed error is nearly 6 r/min.

PI control and robust ILC algorithms have similar current fluctuations, but the robust ILC algorithm shows less speed variation. HFLADRC demonstrates the smoothest speed

Authorized licensed use limited to: NANJING UNIVERSITY OF AERONAUTICS AND ASTRONAUTICS. Downloaded on May 30,2024 at 12:21:51 UTC from IEEE Xplore. Restrictions apply.

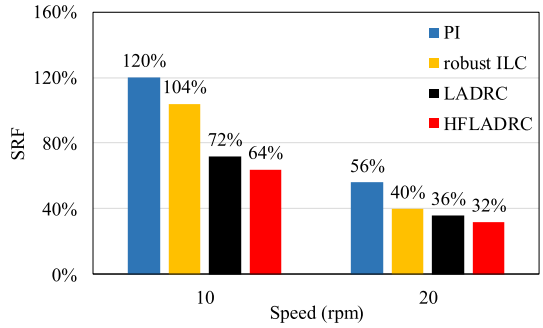

Fig. 16. SRF values of speed for different methods at 10 and 20 r/min.

performance, albeit with relatively higher current fluctuations, to counteract disturbance torque.

It can be seen from the speed spectrum that the main component of the speed harmonics under PI control is 55 times the fundamental harmonic (0.167 Hz), which is consistent with the previous analysis. Although robust ILC does not introduce high-frequency noise, its ability to mitigate periodic disturbances is limited. LADRC can attenuate some speed harmonics, and it also brings in high-frequency disturbances to a certain extent. In contrast, HFLADRC effectively suppresses 55, 110, and 165 times the base frequency while reducing the high-frequency noise caused by the high observer bandwidth.

Fig. 15 shows the experimental performance of different control strategies (PI, robust ILC, LADRC, and HFLADRC) with no load at 20 r/min. When the reference speed is set to 20 r/min, HFLADRC still performs best, followed by robust ILC and LADRC. The q-axis currents of the four strategies are similar to those at 10 r/min. From the speed spectrum, it can, however, be seen that the 110- and 165-times components of the fundamental frequency (0.333 Hz) under LADRC are much higher than that of PI control because more high-frequency noise is introduced by LADRC after the reference speed is increased.

As can be seen from Fig. 16, at the speed of 10 r/min, HFLADRC reduces the SRF from 120%, as observed under PI control, to 64%. Similarly, at 20 r/min, it decreases the SRF from 56% to 32%. The performance ranking, in terms of SRF reduction, is as follows: HFLADRC outperforms LADRC, which is superior to robust ILC, and finally, PI.

Fig. 17 shows the experimental results of four control methods at step speed reference from 10 to 20 r/min; all control strategies show good tracking performance, among which PI control has a relatively small speed overshoot, and LADRC is the largest. Slightly improved performance is observed in the comprehensive evaluation of robust ILC compared to PI. After the reference speed step, the q-axis current of HFLADRC greatly varies because HFLADRC has a good observation of the viscous damping, which is proportional to the speed. The experimental results show that the proposed method can effectively suppress the speed harmonics without introducing high-frequency noise and has good speed adjustment performance. Although HFLADRC introduces some fluctuations in the q-axis current, resulting in a slight decrease in the efficiency of the drive system compared to PI control, this sacrifice is acceptable in light of smooth speed operation.

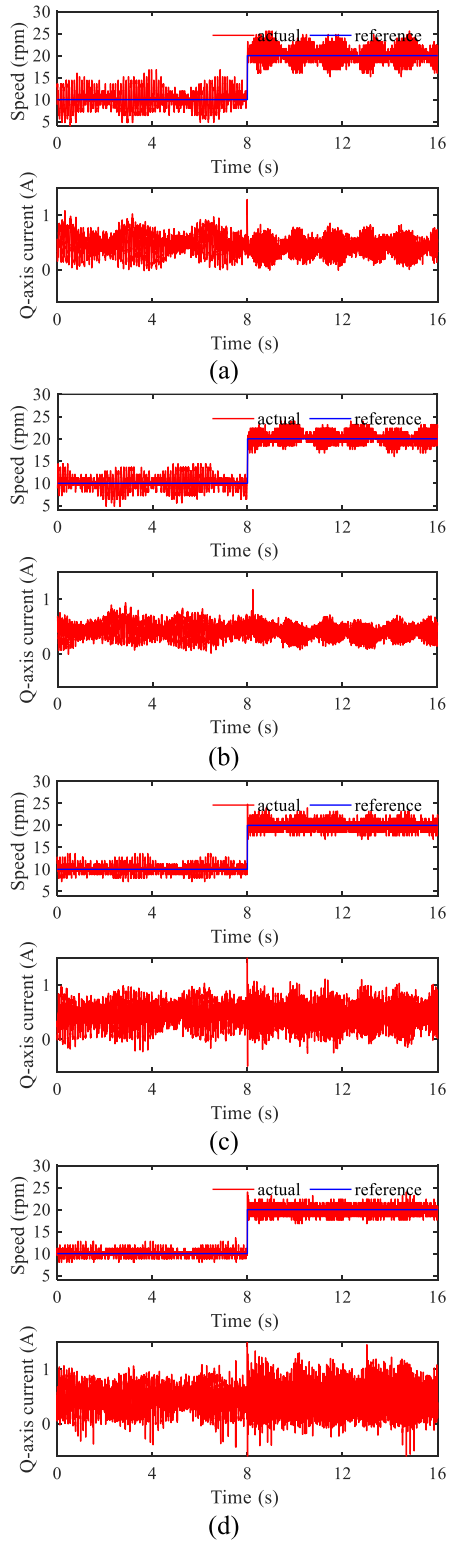

Fig. 17. Experimental results of four control methods at step speed reference. (a) PI, (b) robust ILC, (c) LADRC, and (d) HFLADRC.

VI. Conclusion

This article proposes an improved control strategy for the speed control of PMSM servo systems operating at low speeds.

Authorized licensed use limited to: NANJING UNIVERSITY OF AERONAUTICS AND ASTRONAUTICS. Downloaded on May 30,2024 at 12:21:51 UTC from IEEE Xplore. Restrictions apply.

The proposed control strategy can effectively reduce the speed ripple caused by the periodic disturbances at low-speed operations. The characteristics and effects of offset current error and periodic disturbance of PMSM are analyzed. The principle of parameter design of the strategy is investigated in detail and put forward clearly. The simulation and experimental results of the prototype show that, compared with PI, robust ILC, and LADRC, the proposed control strategy can not only effectively reduce the impact of periodic disturbance torque on speed ripple at low speeds but also has the advantages of simple implementation and strong adaptability.

REFERENCES

[1] P. Pillay and R. Krishnan, "Control characteristics and speed controller design for a high performance permanent magnet synchronous motor drive," *IEEE Trans. Power Electron.*, vol. 5, no. 2, pp. 151–159, Apr. 1990, doi: 10.1109/63.53152.

[2] T. M. Jahns and W. L. Soong, "Pulsating torque minimization techniques for permanent magnet AC motor drives—A review," *IEEE Trans. Ind. Electron.*, vol. 43, no. 2, pp. 321–330, Apr. 1996, doi: 10.1109/41.491356.

[3] D.-M. Park and K.-H. Kim, "Parameter-independent online compensation scheme for dead time and inverter nonlinearity in IPMSM drive through waveform analysis," *IEEE Trans. Ind. Electron.*, vol. 61, no. 2, pp. 701–707, Feb. 2014, doi: 10.1109/TIE.2013.2251737.

[4] A. Houari et al., "An effective compensation technique for speed smoothness at low-speed operation of PMSM drives," *IEEE Trans. Ind. Appl.*, vol. 54, no. 1, pp. 647–655, Jan. 2018, doi: 10.1109/TIA.2017.2740388.

[5] W. Qian, S. K. Panda, and J.-X. Xu, "Torque ripple minimization in PM synchronous motors using iterative learning control," *IEEE Trans. Power Electron.*, vol. 19, no. 2, pp. 272–279, Mar. 2004, doi: 10.1109/tpel.2003.820537.

[6] J. Liu, H. Li, and Y. Deng, "Torque ripple minimization of PMSM based on robust ILC via adaptive sliding mode control," *IEEE Trans. Power Electron.*, vol. 33, no. 4, pp. 3655–3671, Apr. 2018, doi: 10.1109/TPEL.2017.2711098.

[7] C. Xia, B. Ji, and Y. Yan, "Smooth speed control for low-speed high-torque permanent-magnet synchronous motor using proportional-integral-resonant controller," *IEEE Trans. Ind. Electron.*, vol. 62, no. 4, pp. 2123–2134, Apr. 2015, doi: 10.1109/TIE.2014.2354593.

[8] P. Mattavelli, L. Tubiana, and M. Zigliotto, "Torque-ripple reduction in PM synchronous motor drives using repetitive current control," *IEEE Trans. Power Electron.*, vol. 20, no. 6, pp. 1423–1431, Nov. 2005, doi: 10.1109/tpel.2005.857559.

[9] Z. Tang and B. Akin, "Suppression of dead-time distortion through revised repetitive controller in PMSM drives," *IEEE Trans. Energy Convers.*, vol. 32, no. 3, pp. 918–930, Sep. 2017, doi: 10.1109/TEC.2017.2679701.

[10] M. Tang, A. Gaeta, A. Formentini, and P. Zanchetta, "A fractional delay variable frequency repetitive control for torque ripple reduction in PMSMs," *IEEE Trans. Ind. Appl.*, vol. 53, no. 6, pp. 5553–5562, Nov. 2017, doi: 10.1109/TIA.2017.2725824.

[11] J. Han, "From PID to active disturbance rejection control," *IEEE Trans. Ind. Electron.*, vol. 56, no. 3, pp. 900–906, Mar. 2009, doi: 10.1109/tie.2008.2011621.

[12] Z. Gao, "Scaling and bandwidth-parameterization based controller tuning," in *Proc. Amer. Control Conf.*, vol. 6, Jun. 2003, pp. 4989–4996, doi: 10.1109/acc.2003.1242516.

[13] Q. Zheng, L. Q. Gaol, and Z. Gao, "On stability analysis of active disturbance rejection control for nonlinear time-varying plants with unknown dynamics," in *Proc. 46th IEEE Conf. Decis. Control*, Dec. 2007, pp. 3501–3506, doi: 10.1109/cdc.2007.4434676.

[14] S. Li, H. Liu, and S. Ding, "A speed control for a PMSM using finite-time feedback control and disturbance compensation," *Trans. Inst. Meas. Control*, vol. 32, no. 2, pp. 170–187, Apr. 2010, doi: 10.1177/0142331209339860.

[15] A. A. Godbole, J. P. Kolhe, and S. E. Talole, "Performance analysis of generalized extended state observer in tackling sinusoidal disturbances," *IEEE Trans. Control Syst. Technol.*, vol. 21, no. 6, pp. 2212–2223, Nov. 2013, doi: 10.1109/TCST.2012.2231512.

[16] Y. Yan, Z. Sun, and S. Li, "Disturbance rejection control method based on composite disturbance observer for permanent magnet synchronous motor," in *Proc. 41st Annu. Conf. IEEE Ind. Electron. Soc. (IECON)*, Nov. 2015, pp. 3137–3142, doi: 10.1109/IECON.2015.7392582.

[17] W. Xue, W. Bai, S. Yang, K. Song, Y. Huang, and H. Xie, "ADRC with adaptive extended state observer and its application to air-fuel ratio control in gasoline engines," *IEEE Trans. Ind. Electron.*, vol. 62, no. 9, pp. 5847–5857, Sep. 2015, doi: 10.1109/TIE.2015.2435004.

[18] S. Zhu et al., "Robust speed control of electrical drives with reduced ripple using adaptive switching high-order extended state observer," *IEEE Trans. Power Electron.*, vol. 37, no. 2, pp. 2009–2020, Feb. 2022, doi: 10.1109/TPEL.2021.3105263.

[19] Y. X. Su, C. H. Zheng, and B. Y. Duan, "Automatic disturbances rejection controller for precise motion control of permanent-magnet synchronous motors," *IEEE Trans. Ind. Electron.*, vol. 52, no. 3, pp. 814–823, Jun. 2005, doi: 10.1109/TIE.2005.847583.

[20] C. Wang, J. Yan, P. Heng, L. Shan, and X. Zhou, "Enhanced LADRC for permanent magnet synchronous motor with compensation function observer," *IEEE J. Emerg. Sel. Topics Power Electron.*, vol. 11, no. 3, pp. 3424–3434, Jun. 2023, doi: 10.1109/JESTPE.2023.3265686.

[21] H. Li, S. Yang, and Y. Le, "Torque ripple minimization of low-speed gimbal servo system using parameter-optimized ESO," *IEEE J. Emerg. Sel. Topics Power Electron.*, vol. 11, no. 2, pp. 2094–2103, Apr. 2023, doi: 10.1109/JESTPE.2022.3219431.

[22] S. Chai, L. Wang, and E. Rogers, "A cascade MPC control structure for a PMSM with speed ripple minimization," *IEEE Trans. Ind. Electron.*, vol. 60, no. 8, pp. 2978–2987, Aug. 2013, doi: 10.1109/TIE.2012.2201432.

[23] M. Kim, S.-K. Sul, and J. Lee, "Compensation of current measurement error for current-controlled PMSM drives," *IEEE Trans. Ind. Appl.*, vol. 50, no. 5, pp. 3365–3373, Sep. 2014, doi: 10.1109/TIA.2014.2301873.

[24] S. Ye and X. Yao, "An enhanced SMO-based permanent-magnet synchronous machine sensorless drive scheme with current measurement error compensation," *IEEE J. Emerg. Sel. Topics Power Electron.*, vol. 9, no. 4, pp. 4407–4419, Aug. 2021, doi: 10.1109/JESTPE.2020.3038859.

[25] J. Ou, Y. Liu, R. Qu, and M. Doppelbauer, "Experimental and theoretical research on cogging torque of PM synchronous motors considering manufacturing tolerances," *IEEE Trans. Ind. Electron.*, vol. 65, no. 5, pp. 3772–3783, May 2018, doi: 10.1109/TIE.2017.2758760.

[26] W. Qian, S. K. Panda, and J. X. Xu, "Speed ripple minimization in PM synchronous motor using iterative learning control," *IEEE Trans. Energy Convers.*, vol. 20, no. 1, pp. 53–61, Mar. 2005, doi: 10.1109/tec.2004.841513.

[27] S.-K. Chung, H.-S. Kim, C.-G. Kim, and M.-J. Youn, "A new instantaneous torque control of PM synchronous motor for high-performance direct-drive applications," *IEEE Trans. Power Electron.*, vol. 13, no. 3, pp. 388–400, May 1998, doi: 10.1109/63.668096.

[28] Z. Wu, K. Ding, Z. Yang, and G. He, "Analytical prediction and minimization of deadtime-related harmonics in permanent magnet synchronous motor," *IEEE Trans. Ind. Electron.*, vol. 68, no. 9, pp. 7736–7746, Sep. 2021, doi: 10.1109/TIE.2020.3014583.

[29] Z. Song and F. Zhou, "Observer-based predictive vector-resonant current control of permanent magnet synchronous machines," *IEEE Trans. Power Electron.*, vol. 34, no. 6, pp. 5969–5980, Jun. 2019, doi: 10.1109/TPEL.2018.2870904.

Qiangren Xu received the B.Eng. degree in electrical engineering and automation from Southeast University, Nanjing, China, in 2019, and the M.Eng. degree aeronautical and astronautical science and technology from the Shanghai Academy of Spaceflight Technology, Shanghai, China, in 2022. He is currently pursuing the Ph.D. degree in electrical engineering with Southeast University.

His research interests include control strategies for permanent magnet machines and power electronics.

Authorized licensed use limited to: NANJING UNIVERSITY OF AERONAUTICS AND ASTRONAUTICS. Downloaded on May 30,2024 at 12:21:51 UTC from IEEE Xplore. Restrictions apply.

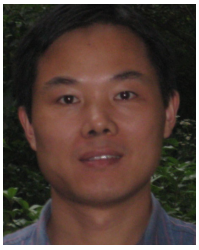

Shuhua Fang (Senior Member, IEEE) received the M.S. degree in electrical engineering from the Shandong University of Science and Technology, Jinan, China, in 2004, and the Ph.D. degree in electrical engineering from Southeast University, Nanjing, China, in 2008.

From 1998 to 2001, he worked as an Associate Engineer at Xuzhou Coal and Mine Machinery Factory, Xuzhou, China, where his research activities were primarily in the area of the design, analysis, and control of electrical apparatus for coal and mine. Since 2008, he has been with Southeast University, where he is currently a Full Professor with the School of Electrical Engineering. From 2013 to 2014, he was a Visiting Professor with the Wisconsin Electric Machine and Power Electronics Consortium (WEMPEC), University of Wisconsin–Madison, Madison, WI, USA. His research interests include design, simulation, and control for both permanent magnet actuators and intelligent apparatus.

Peng Wan received the B.Eng. degree in electrical engineering and automation from Central South University, Changsha, China, in 2019, and the M.S. degree in electrical engineering from Southeast University, Nanjing, China, in 2022.

Since 2022, she has been working as an Engineer with Jiangsu Electric Power Company Maintenance Branch, Nanjing. Her research interests include control strategies for permanent magnet machines, power electronics, and potential transformers.

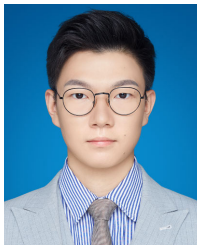

Yicheng Wang received the B.Eng. degree in electrical engineering and automation from Southwest Jiaotong University, Chengdu, China, in 2018, and the M.S. degree in electrical engineering from Southeast University, Nanjing, China, in 2021, where he is currently pursuing the Ph.D. degree in electrical engineering.

His research interests include control strategies for permanent magnet machines and power electronics.

Demin Huang received the B.Eng. degree in electrical engineering and automation from the Nanjing Institute of Technology, Nanjing, China, in 2020, and the M.S. degree in electrical engineering from Southeast University, Nanjing, in 2023.

He is currently a Motor Control Algorithm Engineer in Inovance, Nanjing, where he has been working as an Engineer, since 2023. His research interests include control strategies for permanent magnet machines, power electronics, and potential transformers.

Authorized licensed use limited to: NANJING UNIVERSITY OF AERONAUTICS AND ASTRONAUTICS. Downloaded on May 30,2024 at 12:21:51 UTC from IEEE Xplore. Restrictions apply.